Acta Med. Okayama, 2021
Vol. 75, No. 2, pp. 187–197

Acta Medica Okayama
http://escholarship.lib.okayama-u.ac.jp/amo/

Original Article

Multiacquisition Variable-Resonance Image Combination Selective Can Improve Image Quality and Reproducibility for Metallic Implants in the Lumbar Spine

Yuta Fujiwara[a], Tomoaki Sasaki[b]*, Yuki Muto[b], Masaki Hirano[b], Ryo Kamizaki[c], Kaito Murakami[c], Naoya Miura[c], Yutaka Fujibuchi[c], Nayu Ohmukai[c], Nao Ueda[c], Kouhei Sugimoto[b], Kazuhiro Ota[a], Yoshiki Kamihoriuchi[a], Tomoko Sasaki[a], and Souichirou Kaneshige[d]

[a]Division of Clinical Radiology Service, [d]Department of Radiology, Okayama Central Hospital, Okayama 700-0017, Japan, Department of Radiological Technology, [b]Graduate School of Health Sciences, [c]Faculty of Health Sciences, Okayama University, Okayama 700-8558, Japan

The aim of this study is to evaluate how metallic artifacts in the lumbar spine can affect images obtained from magnetic resonance (MR) sequences. We performed a phantom experiment by scanning an agar containing an orthopedic metallic implant using 64-channel multidetector row computed tomography (CT) and a 3-tesla MR unit. We compared the reproducibility in each measurement, enlargement or reduction ratio of the CT and MR measurements, and signal deviation in each voxel from the control. The reproducibility on CT and multiacquisition variable-resonance image combination selective (MAVRIC SL) was good, but that on the other MR sequences showed either fixed bias or proportional bias. The reduction ratios of the distance between the nails were significantly smaller in MAVRIC SL than in the other MR sequences after CT measurements ($p < 0.001$, respectively). MAVRIC SL was able to reduce the metallic artifact, permitting observation of the tissue surrounding the metal with good reproducibility.

Key words: metallic artifact reduction, implant, MAVRIC SL

Magnetic resonance imaging (MRI) enables us to observe human tissues with excellent contrast. However, metallic devices can changes the signals during the imaging process, resulting in distortion of the structures in the MRI images, and can also cause harmful events related to heat production or movement of the metal [1].

Several methods are available to adjust the scan parameters to minimize susceptibility artifacts in MRI: decreasing the echo time, increasing the readout bandwidth, increasing the matrix sizes, and decreasing the slice thickness [1,2]. Adjusting the readout direction is also effective to reduce artifacts on a plane [1,3-5]. Alternatively, several methods have also been developed to correct the metallic artifacts after they develop. For example, view-angle-tilting (VAT) can be used to correct the in-plane acquiring slice-selection gradient again with the conventional readout gradient [1,6]. Slice-encoding for metal artifact correction (SEMAC) is a method which extends VAT to allow for correction of both through-plane distortion and in-plane distortion [1,7]. Multiacquisition variable-resonance image combination (MAVRIC) is a method to composite informa-

Received August 17, 2020; accepted November 30, 2020.
*Corresponding author. Phone: +81-86-235-6867; Fax: +81-86-222-3717
E-mail: tsasaki-rad@okayama-u.ac.jp (T. Sasaki)

Conflict of Interest Disclosures: No potential conflict of interest relevant to this article was reported.

tion of off-resonant frequency near metal acquiring various radio frequency offsets [1,3]. A method combining MAVRIC and SEMAC, called multiacquisition variable-resonance image combination selective (MAVRIC SL), has been embedded into a clinical apparatus [1].

The surgical insertion of metal implants in the field of orthopedics has improved the quality of life of patients with fracture or degenerative changes in joints. However, postoperative complications can include hematoma, infection or aseptic loosening at the surgical site [1]. In such cases, X-ray and CT are first used to observe the surgical sites, but their diagnostic accuracy is often not sufficient in the event of complications [8]. Nuclear medicine examinations such as bone scintigraphy can be used, but they have limited spatial resolution and can result in non-specific accumulation of radioisotope [8]. Positron emission topography (PET)/CT may show a pseudopositive result by accumulation of the radioisotope in granuloma or postoperative change [8-10]. In the case of MRI, the diagnosis of complications can be difficult because the metallic implants themselves can hamper the observation of conditions at the surgical site.

When using MRI to clinically diagnose complications following the surgical insertion of a metallic implant, it is important to adjust the scan parameters to minimize the metallic artifacts [1,11,12]. Numerous studies have reported that a metallic artifact reduction sequence including MAVRIC SL can yield better image quality after hip or knee joint arthroplasty compared to fast spin echo sequences [1,3,5,11-15]. To the best of our knowledge, however, there have been few reports about the reduction of susceptibility artifacts by adding MAVRIC SL to MRI when imaging metallic implants of the lumbar spine. Kaushik *et al.* demonstrated that three-dimensional multispectral imaging reduced the metallic artifacts from lumbar implants, and suggested that it might be also important to have the capacity to evaluate the surrounding structures, such as the nerve roots, disks, and spinal cord [16,17]. The aim of this study was to compare the amount of metallic artifact reduction achieved by MAVRIC SL in comparison with other MR sequences and to ascertain whether metal artifact reductions affect the reproducibility of measurement and the assessment of soft tissue surrounding the metal.

Materials and Methods

Phantom. We established an agar phantom using 0.9% sodium in a box of 280×190×145 mm. We then placed a metallic implant made from 2 long bars of 100% titanium with 3 nails in each into the phantom. We set two syringes, one including oil and the other including agar of the same composition as in the phantom, near the main phantom for scanning.

Imaging study. We scanned the phantom using a CS-7 X-ray system (Konica Minolta, Inc, Tokyo, Japan). The parameters were as follows: matrix size 1,722×1,430, tube voltage 120 kVp, and tube current 40 mA. Next, we obtained computed tomography (CT) images using a 64-channel multidetector row CT system (Sensation 64; Siemens, Erlangen, Germany). The scanning parameters were as follows: tube voltage 140 kVp automated tube current modulation = on; detector collimation, 0.6×64 mm; helical pitch, 32; reconstructed by 512×512 pixels. We used a 3.0 Tesla MR apparatus (3.0T SIGNA Architect ver 26.1; General Electric, Milwaukee, WI, USA). A posterior array coil and an anterior array coil were used. We scanned the phantom three times using clinically available sequences: MAVRIC SL, a three-dimensional fast spin echo extended echo train acquisition method known as Cube, and magnetic resonance image complication (MAGiC). The image contrast was adjusted close to proton-density weighted. The scan parameters are shown in Table 1.

Image analysis. All image analyses were done by a commercially available software package (MATLAB 2020a; MathWorks, Natick, MA, USA). We evaluated two X-ray images without the direct measurements of the nails and distance between the nails in each depth of the nail to calculate references of nails and distance between nails (Fig. 1). This is because the skeletal tissue around nails, not tissue around the nail bases, after orthopedic surgery should be evaluated. First, two of us independently selected 15 out of a maximum of 35 locations for the base and 50 out of 201 locations for the nail on the oblique X-ray image (dotted lines in Figs. 1A and 1B). After the selection, the MATLAB software automatically generated a plot graph with two peaks of bases or six peaks of nails (Fig. 1B). Each base or nail diameter was determined as the full width at half maximum (FWHM). The values were averaged for analysis. Second, the same two individuals selected 15 out of a

Table 1 Scan parameters in each MR sequence

	MAVRIC SL	Cube	MAGiC
TR/TE	3000/6.3	3002/14	MDME 4000–5600/23–95
FOV	30	30	30
Matrix size	256 × 256	320 × 320	320 × 192
Slice thickness	1.4 mm	0.9 mm	1.8 mm
Flip angle	60	NA	NA
ARC	Phase: 3.0 Slice: 2.0	Phase: 2.5 Slice: 2.0	Phase: 2.25
Echo train length	20	60	16
Frequency direction	S/I	S/I	S/I
Echo spacing	6.3	4.7	10.0
Band width/pixel	976.6 Hz	488.3 Hz	156.2 Hz
Scan time	5:06	5:10	4:51
Others			Automatically calculated 4 Different inversion recovery time

*MDME: multi-delay multi echo.

maximum 53 locations on the X-ray (Fig. 1C), and then 2 peaks as the bases were obtained. Using half of the peak value, we created binary images to measure the bases and the distance between the bases (Fig. 1D). We also measured the diameters of the nail bases in the 2 central bases in the Fig. 1A (arrow) due to the good separation on the image to calculate the ratios of nail to base (Fig. 1E). Third, using the ratios of nail to base, the diameters of bases, and the distance between bases we obtained the distance between nails (Fig. 1E). Subsequently, 2 of us independently measured the distances of both nails and distances between the nails in 15 locations for CT or an MRI sequence. The registration of the depth of the nails was almost perfectly made by consensus of at least 2 readers using a commercially available DICOM viewer (RadiAnt DICOM Viewer 5.51; Medixant, Poland) (Fig. 2). We defined the diameters of the nail on X-ray and CT as each width of 2 signal peaks and the distances between the nails as the width connecting inner borders of each nail in the right-left directions (Fig. 1B and Figs. 3A and 3B). We first defined the distances between the nails as the full width at half maximum (FWHM) between the large 2 signal valleys equivalent to the 2 nails. Second, the half maximum value of FWHM was used for the outer borders of each nail (Figs. 3C to 3H): the diameters of the nail on MRI were considered to be the widths connecting the half maximum values in the 2 signal valleys. The coordinate information of the inner border of the nails was recorded for the last evaluation.

Next, we segmented the control syringe in the center slice of the whole phantom for the control agar signal and the volume data of the whole phantom in each sequence (Fig. 4). We averaged the signal values in the control syringe as the "mean value." The signal deviation (SD) in each voxel of the whole volume was compared to the mean value using the following formula:

signal deviation (SD) = (signal in each voxel – mean value)/mean value

We calculated the mean values, standard deviation, skewness, and kurtosis of the SD in the whole phantom. Finally, we segmented the volume of the phantom inside the dotted rectangle which was drawn by the information of the locations of the inner border of the nails (Fig. 4A), in order to simulate the location of the dural sac, peripheral nerves, and spinal cord for spinal MRI. For evaluation of the lumbar implants, in addition to the infection or inflammation near the metal, we

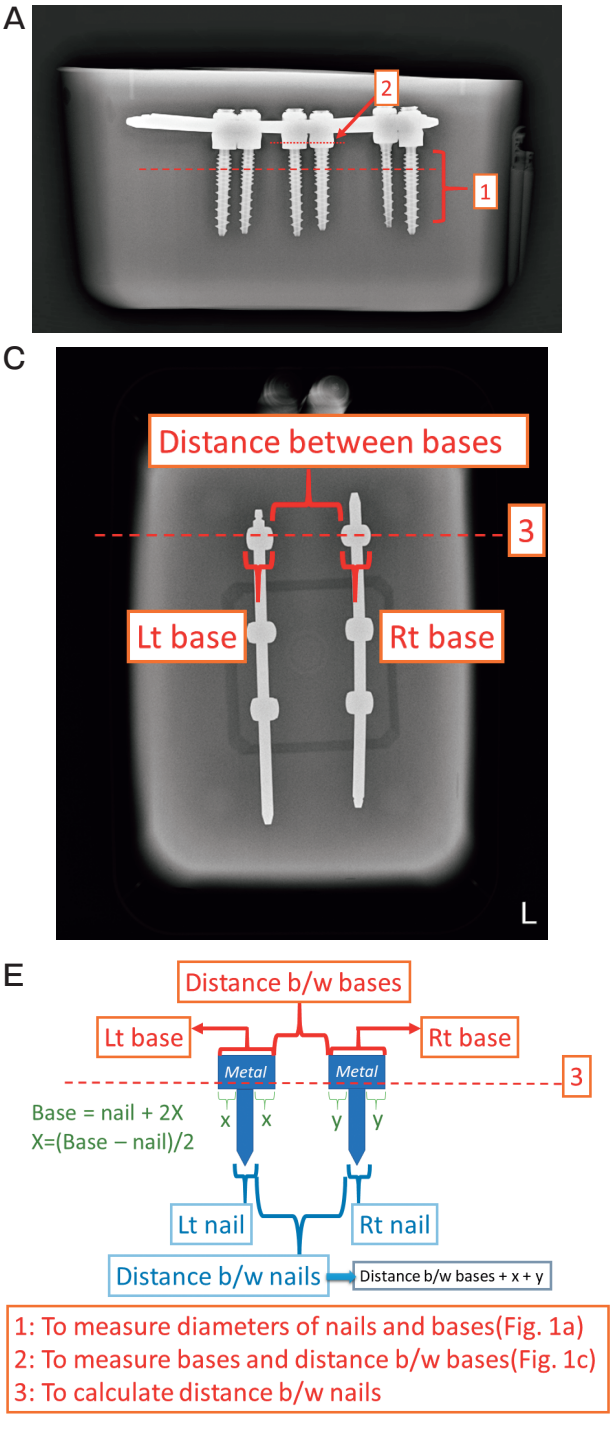

Fig. 1 **A**) An oblique lateral view of an X-ray image showing six nails, *i.e.*, 3 in each of 2 metallic bars in the phantom. First, the diameters of the 6 nails were measured at several heights. Second, the diameters of the nail bases in the 2 central bases were measured (arrow) due to the good separation on the image; **B**) A graph showing a plot on the dotted line in Fig. 1A. There are 6 peaks in the range from location 600 to location 1300, corresponding to the 6 nails in Fig. 1A. The mean value of the six peaks can be calculated, and then the diameter of each nail can be determined by using the full width at half maximum (FWHM) as a cutoff value; **C**) A vertical view of an X-ray image showing the two metallic bars with 3 nail bottoms in each; **D**) A binary image of Fig. 1C after determining the cutoff value in the same manner as in Fig. 1B (not shown). We can measure the "Lt base", "Distance between bases", and "Rt base"; **E**) A lateral view of the image in panel (c), showing the relation between the base and nail. We can calculate the "Lt nail", "Distance between nails", and "Rt nail".

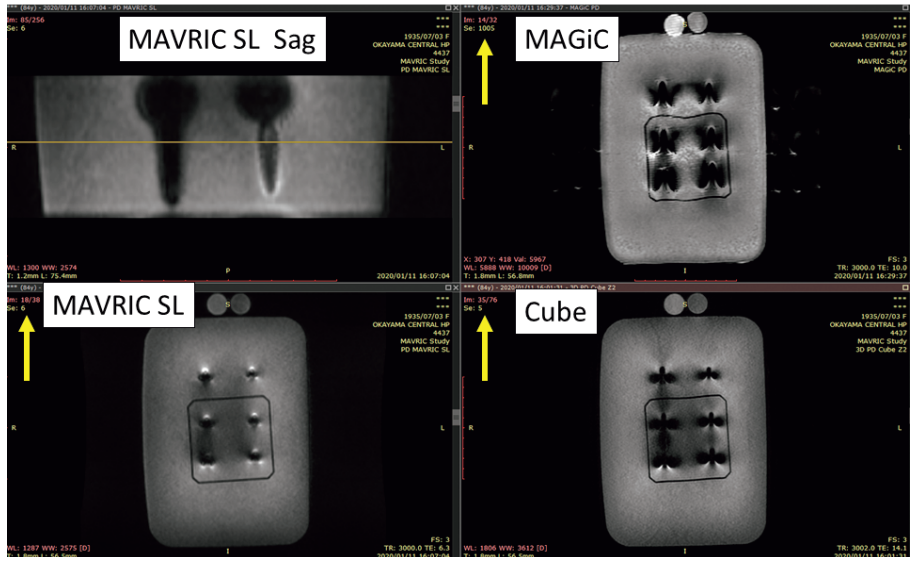

Fig. 2 Cross reference lines in each MR sequence were automatically generated using RadiAnt DICOM Viewer. Each window showed the slice location in each MR sequence (arrows).

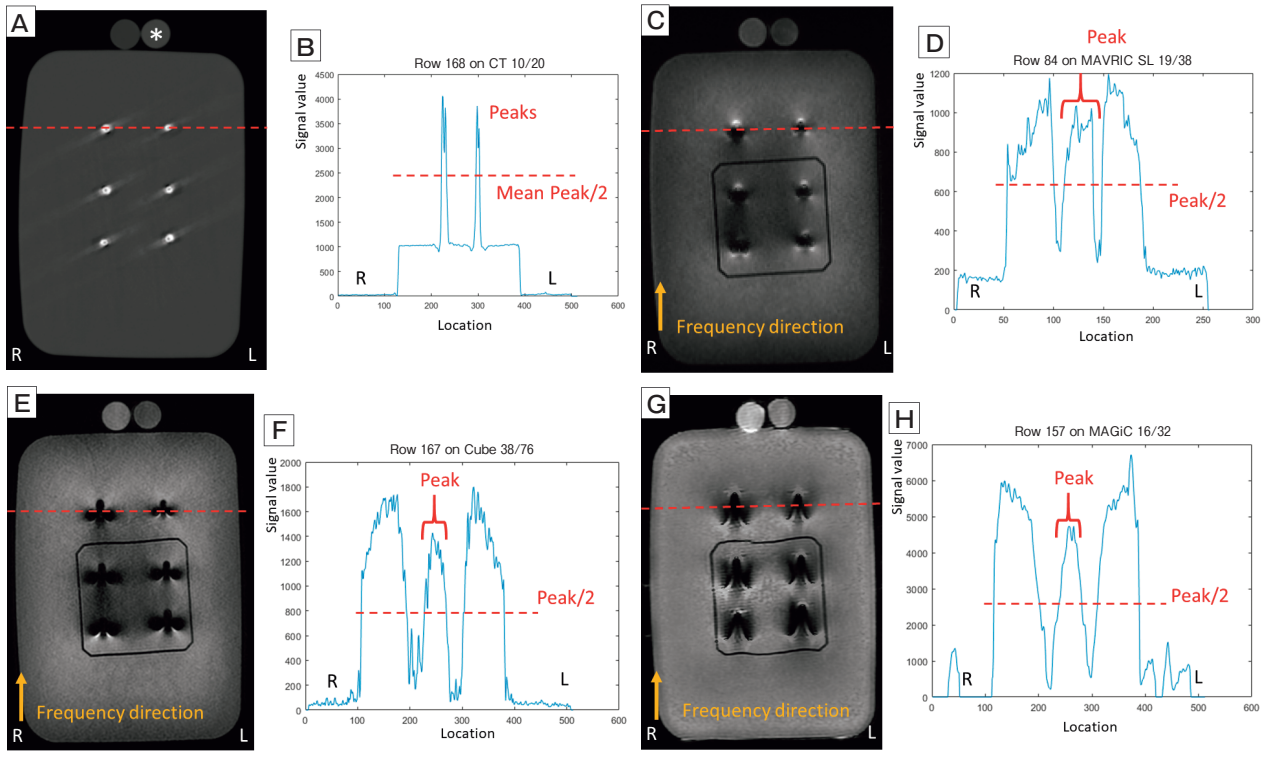

Fig. 3 The 6 nails in the phantom were observed on (**A**) CT, (**C**) MAVRIC SL, (**E**) Cube, and (**G**) MAGiC. Horizontal dotted lines were drawn on the 2 nails so that signals on the images were plotted for each image: (**B**) CT, (**D**) MAVRIC SL, (**F**) Cube, and (**H**) MAGiC. On CT, the 2 peaks of signals correspond to the nails. The diameters of the nails were determined by the FWHM method, and then the distance between the nails was calculated. In MRI images (**D**), (**F**), and (**H**), the distance between the nails was determined by the peak in the center, then the diameters of the nails were determined. *An asterisk indicated the control syringe with agar of the same composition.

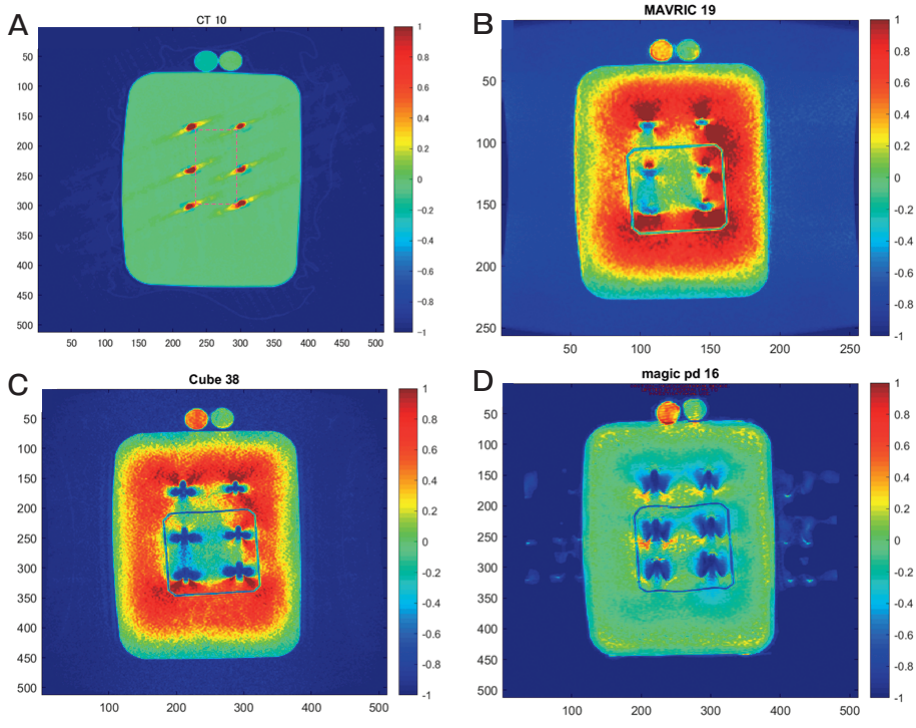

Fig. 4 Images showing the signal deviation (SD) based on the mean value of the agar signal in the control syringe (arrow): (A) CT, (B) MAVRIC SL, (C) Cube, and (D) MAGiC. Red means increased signals compared to the mean, but blue means decreased signals. The dotted rectangle is used for the analyses in Fig. 6.

should also evaluate how much the metallic artifact could affect the image quality rectangle. The location of the rectangle was defined by the former coordinate information of the inner border of each nail on the software.

Statistics. The statistical analysis was performed using MATLAB 2020a and SPSS version 25 (IBM Corporation, Armonk, NY, USA). Measurements, such as the diameters of the nails and distance between nails, obtained by the two individuals, were assessed by Bland-Altman plots [18-22]. After averaging the 2 measurements, we calculated the enlargement ratios for (1) the left nails, and (2) the right nails, and the reduction ratio for the distances between nails in X-ray measurements from CT or MR measurements using the following formula:

$$\text{enlargement ratio for nails} = (\text{length}_{\text{CT/MRI}} - \text{length}_{\text{X-ray}})/\text{length}_{\text{Xray}}$$

$$\text{reduction ratio for distance between nails} = (\text{length}_{\text{CT/MRI}} - \text{length}_{\text{X-ray}})/\text{length}_{\text{Xray}}$$

Here, length is the averaged measurement by 2 readers in each image. We compared the averaged measurements among the different sequences using one-way analysis of variance (ANOVA) and multiple comparison with Games-Howell correction after a Shapiro-Wilk test. In addition, we compared SDs in the whole phantom and rectangle using the Kruskal-Wallis test and Mann-Whitney test with Bonferroni correction as a post hoc test. The ratios of rectangular volume inside the nails to the whole phantom volume were compared using the chi-square test with Bonferroni correction. The ratio of the volume rectangle to the whole phantom volume should depend on the metallic artifact from the nails. If the metallic artifact is larger, the rectangle will be smaller since the inner border of the nail must be plotted inside. A p value of < 0.05 was considered statistically significant.

Results

Reproducibility evaluation. Bland-Altman plots demonstrated no significant fixed biases ($p = 0.260$ to 0.823 in X-ray, $p = 0.082$ to 0.499 in CT, $p = 0.233$ to 0.625, in MAVRIC SL, respectively) and proportional biases ($p = 0.054$ to 0.803 in X-ray, $p = 0.523$ to 0.742 in CT, $p = 0.075$ to 0.164, in MAVRIC SL, respectively).

There were significant fixed biases ($p < 0.001$ in the all the measurements by MAGiC, $p < 0.001$ to 0.02 in the all the measurements by Cube, respectively). In Cube, there was also a significant proportional bias in the distance between nails ($p = 0.037$). However, there were no significant proportional biases ($p = 0.199$ to 0.729 in all the measurements by MAGiC, $p = 0.120$ to 0.220 in the diameters of the left and right nails in Cube, respectively).

Comparisons of images. The X-ray image showed that the diameter of the left nail was 5.64 mm, the diameter of the right nail was 6.12 mm, and the distance between the nails was 42.99 mm.

The null hypothesis was not rejected by the Shapiro-Wilk test in the CT or MR sequence ($p = 0.121$ to 0.944). The enlargement ratios are shown in Table 2. In the left and right nails, the enlargement ratio of CT was significantly smaller than those three MR sequences ($p < 0.001$ in MAVRIC SL, $p < 0.001$ in Cube, $p < 0.001$ in MAGiC). Moreover, the enlargement ratio in MAVRIC SL was smaller than those in Cube and MAGiC ($p < 0.001$ in Cube, $p < 0.001$ in MAGiC). There were no significant differences in the enlargement ratios between Cube and MAGiC.

In regard to the distance between the nails, the reduction ratio of CT was significantly smaller than those three MR sequences ($p < 0.001$ in MAVRIC SL, $p < 0.001$ in Cube, $p < 0.001$ in MAGiC). In addition, the reduction ratio in MAVRIC SL was smaller than those in Cube and MAGiC ($p < 0.001$ in Cube, $p < 0.001$ in MAGiC). There was no significant difference between Cube and MAGiC.

Signal deviation (SD) analysis. Table 2 shows the results of the SDs in each sequence. The SDs in the whole phantom were significantly higher in MAVRIC SL than in Cube and MAGiC ($p < 0.001$, and $p < 0.001$, respectively; Fig. 5). However, the histograms of the SDs of the whole phantom on Cube and MAGiC

Table 2 Enlargement ratios and signal deviations in CT and MR sequences

	MAVRIC SL	Cube	MAGiC	CT
Lt nail	1.24 +/− 0.587**	2.84 +/− 0.631*, **	2.90 +/− 0.759*, **	0.133 +/− 0.235
Distance between nails	−0.179 +/− 0.346**	−0.462 +/− 0.0991*, **	−0.456 +/− 0.104*, **	−0.0768 +/− 0.0323
Rt nail	0.431 +/− 0.209**	2.54 +/− 0.733*, **	2.65 +/− 0.816*, **	−0.0940 +/− 0.239
Signal deviations (SDs) of whole phantom				
Mean +/− standard deviation	0.405 +/− 0.511 §	0.168 +/− 0.467 §	−0.168 +/− 0.279 §	0.000 +/− 0.265 §
Skewness	0.722	−0.389	−1.522	8.787
Kurtosis	6.384	3.136	5.031	92.42
SDs inside of the nails				
Ratios of volume inside nails	10.05% †	7.58% †	8.96% †	10.98% †
Mean +/− standard deviation	0.200 +/− 0.522 §	−0.133 +/− 0.451 §	−0.323 +/− 0.358 §	0.028 +/− 0.364 §
Skewness	0.216	−0.095	−0.390	5.480
Kurtosis	2.149	1.889	2.350	43.22

* significantly difference compared to MAVRIC SL, $P < 0.001$ (Multiple comparison with Games-Howell correction).
** significantly difference compared to CT, $P < 0.001$ (Multiple comparison with Games-Howell correction).
§ significantly differences compared to others, $P < 0.001$ (Mann-Whitney test with Bonferroni correction).
† significantly differences compared to others, $P < 0.001$ (Chi-square test with Bonferroni correction).

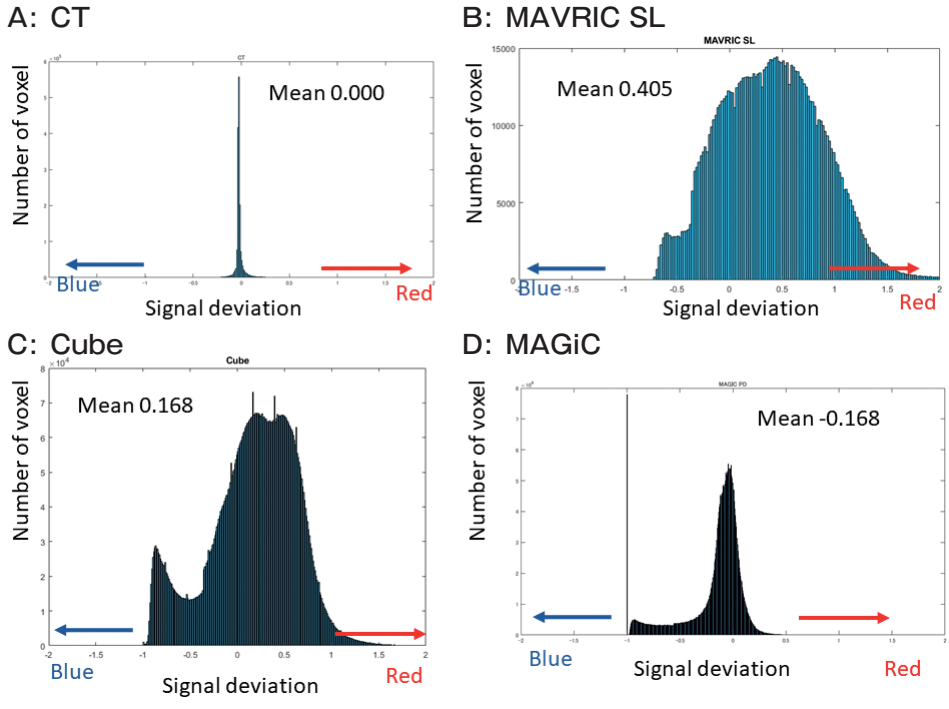

Fig. 5 Histogram charts for the whole agar in each image: (**A**) CT, (**B**) MAVRIC SL, (**C**) Cube, and (**D**) MAGiC. Zero means no signal deviation (SD) from control agar signals. There was less SD on CT. There was no peak around minus one on MAVRIC SL, suggesting fewer voxels of signal loss due to metallic artifacts. Both (**C**) Cube and (**D**) MAGiC show signal deviations around minus 1, suggesting signal loss due to the metallic artifact (Figs. 3E and 3G).

showed negative skewnesses, which was affected by the increased number of signal loss (around minus one) volume.

In addition, the ratio of volume inside the rectangle on MAVRIC SL was 10.05%, which was significantly higher than those on MAGiC and Cube ($p < 0.001$, and $p < 0.001$, respectively). The histograms of the SDs inside the rectangle revealed the significantly lower mean SDs on Cube and MAGiC compared to that on MAVRIC SL and the negative skewness on the Cube and MAGiC values (Fig. 6).

Discussion

Our data showed good reproducibility of the measurements for X-ray, CT, and MAVRIC SL, but either fixed or proportional bias was observed in Cube and MAGiC. MAVRIC SL demonstrated the smallest measurement errors among the three MR sequences. In the comparison with the other MR sequences, MAVRIC SL was able to reduce the metallic artifact of 1 to 2 nail diameters, resulting in the smallest reduction ratio of the distance between nails (Fig. 7). In addition, the ratio of the volume inside the rectangle was the largest and the preservation of the signals was greatest in MAVRIC SL compared to the other MR sequences. We should pay attention to the SDs inside the rectangle compared to those of the whole phantom when evaluating the spine. The volume inside the rectangle was implied to be the location of the dural sac, nerve roots, and spinal cord, where MRI could evaluate with higher accuracy compared to CT or X-ray. As a result, MAVRIC SL could better observe not only the tissue close to the nails, such as in complications of metal implant, abscess or hematoma, but also the tissue between the nails, such as in secondary disc herniation, nerve root compression, or spinal cord injury [1]. Although SEMAC formed a half of the susceptibility artifact reduction mechanism of MAVRIC SL, SEMAC enabled us to observe fluid collection near the metal [1]. In the future, MAVRIC SL might contribute to an improvement in diagnostic accuracy in a human study.

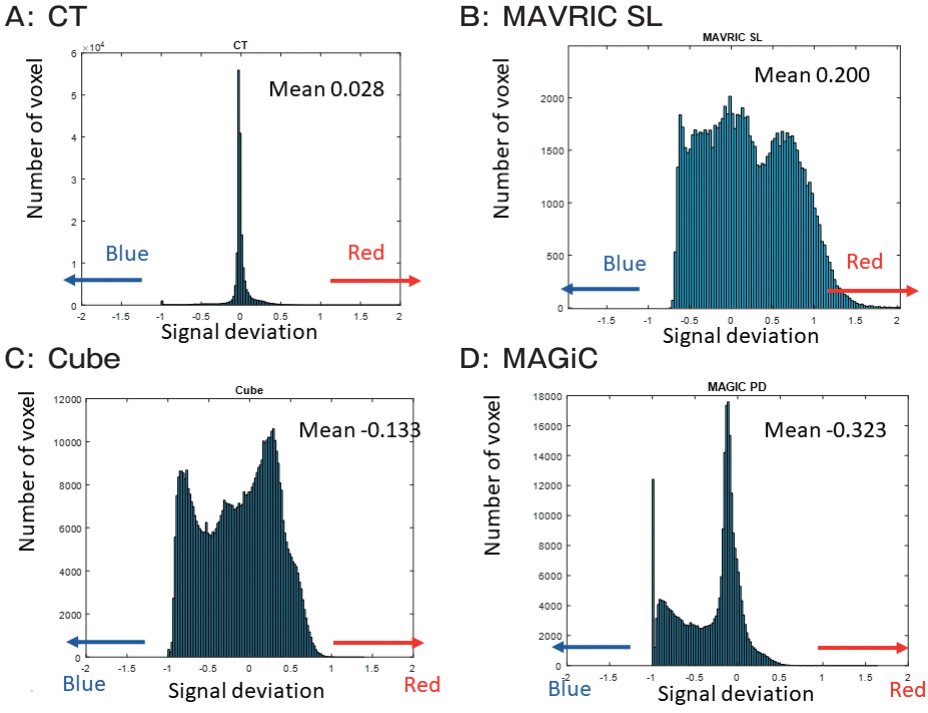

Fig. 6 These charts illustrate the histograms inside the rectangle in Fig. 4A. (A) CT, (B) MAVRIC SL, (C) Cube, and (D) MAGiC. There were peaks around minus one on Cube and MAGiC, resulting in the lower mean SDs and negative skewness. However, MAVRIC SL was able to preserve the SDs around zero despite the signals inside the rectangle.

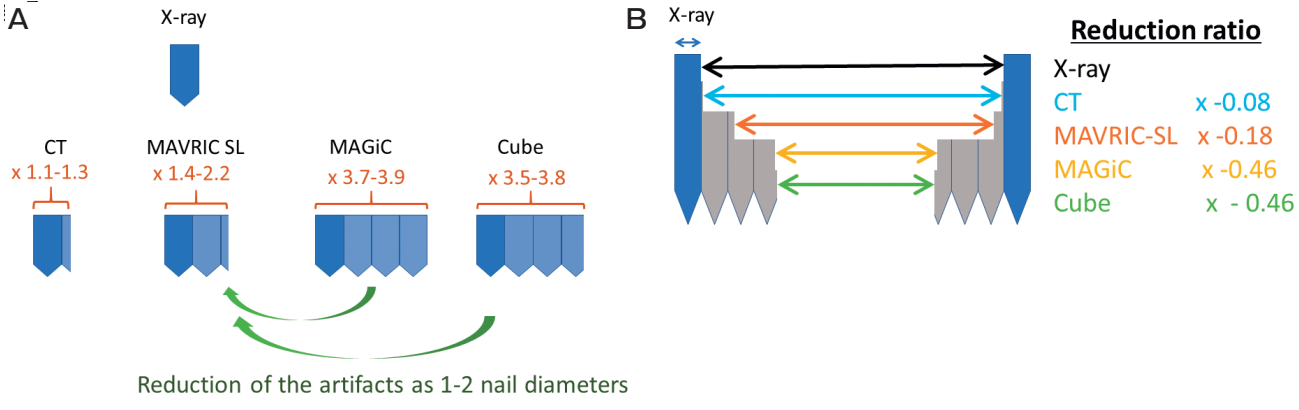

Fig. 7 Illustrations showing (A) how much the diameter of one nail on an X-ray image is visualized as enlarged on CT or each MR sequence. Adding MAVRIC SL enables us to observe the inside of 1 to 2 nails as width that could not be seen on Cube or MAGiC, and (B) how much the distance between the nails would be reduced on CT or each MR sequence. MAVRIC SL enables us to observe with good reproducibility more about 24% of the X-ray diameter compared to MAGiC and Cube.

Adjusting the readout direction is important for reducing susceptibility artifacts in direction [1,5]. We compared the enlargement ratios only in the phase direction (R-L direction) after adjusting the S-I direction as a readout direction. Previous studies have shown that avoiding the readout direction is the best way to minimize the metallic artifact in one direction [1,5]. It is common in a clinical situation to adjust the

readout direction in order to evaluate chemical shift artifacts, such as those from dermoid cysts in an ovarian tumor [23, 24]. Therefore, it is reasonable to evaluate the artifacts after adding the same sequence with a different readout direction if needed. We interpreted MAVRIC SL had an advantage for reducing susceptibility artifacts due to (1) short echo time, (2) high pitch of readout band width, (3) multiple off-resonance pulse to correct information dephasing due to metal, and (4) misalignment correction for readout gradient. The sequence successfully reduced the number of blacked out voxels in comparison to that by the other MR sequences. This is because dephased proton signals due to metallic implant can induce signal loss on the plane image. Therefore, MAVRIC SL might be useful for evaluating fluid collection or an abscess near the metallic device with high reliability. However, MAVRIC SL has several limitations, namely: (1) a low signal-to-noise ratio leading to 256×256, (2) limited sequences, *i.e.*, no long echo time sequence, such as T2 weighted imaging or short echo time inversion recovery, is available in this version of the software. In addition, our results suggested that the MR signal shift was higher than that of the control.

MAGiC, a synthetic MR sequence, is now available [25, 26]. The data set was obtained with the multi repetition time, echo time and inversion recovery time. Therefore, the sequence can contain the short echo time information, which would lead to a reduction in susceptibility artifacts. However, we had no other choice but to use a low readout band width of 250 Hz/pixel. This may be associated with reduced MRI signals in the whole voxels. A three-dimensional fast spin echo sequence using variable flip angles, such as Cube, can be used for cisternography in the spine, especially in the long repetition time and echo time settings. Neither MAGiC nor Cube used the technique reducing susceptibility artifacts, which resulted in decreased reproducibility.

Our study has several limitations. First, scan parameters, such as matrix size, slice thickness, and band width, were different among the sequences we acquired. However, this is common in clinical situations, and each sequence should be scanned for a specific purpose in cases in which the total examination time is limited. Second, we were not able to measure the actual diameters of the nails. There were differences of the distances to the detector from the 6 nails and rough surfaces in themselves. We believe that we were able to reduce the differences related to the enlargement effect on X-rays by using the mean of the 6 nails. In addition, the finding that the difference of the enlargement ratio was smallest on CT meant that the measurement errors due to the distance between the detector and each nail on the X-ray image and CT was much smaller than those due to tha metal artifact of MRI. Using the mean measurements at 50 locations per nail could reduce the measurement error due to the shape of unevenness of the nail. Third, we used the MR measurements of Cube and MAGiC for comparison, even though we were not able to prove their reproducibility. However, in terms of our initial hypothesis, it seems reasonable to conclude that MAVRIC SL was able to improve the reproducibility. Fourth, since this was a phantom experiment, we should wait for the results of a clinical study before concluding that our method is truly clinically useful. However, we are hopeful that our results will encourage future clinical studies.

In conclusion, MAVRIC SL reduced metallic artifacts from metal implants with good reproducibility, indicating that this sequence might have potential for the accurate diagnosis of complications involving tissues or lesions in close proximity to metal implants.

Acknowledgments. This work was supported by the Japan Society for the Promotion of Science Grant-in-Aid for Scientific Research Grant No. 20K08136 (Tomoaki Sasaki).

References

1. Jungmann PM, Agten CA, Pfirrmann CW and Sutter R: Advances in MRI around metal. J Magn Reson Imaging (2017) 46: 972–991.
2. Viano AM, Gronemeyer SA, Haliloglu M and Hoffer FA: Improved MR imaging for patients with metallic implants. Magn Reson Imaging (2000) 18: 287–295.
3. Koch KM, Brau AC, Chen W, Gold GE, Hargreaves BA, Koff M, McKinnon GC, Potter HG and King KF: Imaging near metal with a MAVRIC-SEMAC hybrid. Magn Reson Med (2011) 65: 71–82.
4. Koch KM, Lorbiecki JE, Hinks RS and King KF: A multispectral three-dimensional acquisition technique for imaging near metal implants. Magn Reson Med (2009) 61: 381–390.
5. Smith MR, Artz NS, Wiens C, Hernando D and Reeder SB: Characterizing the limits of MRI near metallic prostheses. Magn Reson Med (2015) 74: 1564–1573.
6. Butts K, Pauly JM and Gold GE: Reduction of blurring in view angle tilting MRI. Magn Reson Med (2005) 53: 418–424.
7. Lu W, Pauly KB, Gold GE, Pauly JM and Hargreaves BA: Slice encoding for metal artifact correction with noise reduction. Magn Reson Med (2011) 65: 1352–1357.
8. Cyteval C and Bourdon A: Imaging orthopedic implant infections.

Diagn Interv Imaging (2012) 93: 547–557.
9. Bhoil A, Caw H and Vinjamuri S: Role of 18F-flurodeoxyglucose in orthopaedic implant-related infection: review of literature and experience. Nucl Med Commun (2019) 40: 875–887.
10. Wenter V, Müller JP, Albert NL, Lehner S, Fendler WP, Bartenstein P, Cyran CC, Friederichs J, Militz M, Hacker M and Hungerer S: The diagnostic value of [(18)F]FDG PET for the detection of chronic osteomyelitis and implant-associated infection. Eur J Nucl Med Mol Imaging (2016) 43: 749–761.
11. Choi SJ, Koch KM, Hargreaves BA, Stevens KJ and Gold GE: Metal artifact reduction with MAVRIC SL at 3-T MRI in patients with hip arthroplasty. AJR Am J Roentgenol (2015) 204: 140–147.
12. Kretzschmar M, Nardo L, Han MM, Heilmeier U, Sam C, Joseph GB, Koch KM, Krug R and Link TM: Metal artefact suppression at 3 T MRI: comparison of MAVRIC-SL with conventional fast spin echo sequences in patients with Hip joint arthroplasty. Eur Radiol (2015) 25: 2403–2411.
13. Hargreaves BA, Worters PW, Pauly KB, Pauly JM, Koch KM and Gold GE: Metal-induced artifacts in MRI. AJR Am J Roentgenol (2011) 197: 547–555.
14. Ai T, Padua A, Goerner F, Nittka M, Gugala Z, Jadhav S, Trelles M, Johnson RF, Lindsey RW, Li X and Runge VM: SEMAC-VAT and MSVAT-SPACE sequence strategies for metal artifact reduction in 1.5T magnetic resonance imaging. Invest Radiol (2012) 47: 267–276.
15. Ariyanayagam T, Malcolm PN and Toms AP: Advances in Metal Artifact Reduction Techniques for Periprosthetic Soft Tissue Imaging. Semin Musculoskelet Radiol (2015) 19: 328–334.
16. Kaushik SS, Marszalkowski C and Koch KM: External calibration of the spectral coverage for three-dimensional multispectral MRI. Magn Reson Med (2016) 76: 1494–1503.
17. Kaushik SS, Karr R, Runquist M, Marszalkowski C, Sharma A, Rand SD, Maiman D and Koch KM: Quantifying metal-induced susceptibility artifacts of the instrumented spine at 1.5T using fast-spin echo and 3D-multispectral MRI. J Magn Reson Imaging (2017) 45: 51–58.
18. Bland JM and Altman DG: Statistical methods for assessing agreement between two methods of clinical measurement. Lancet (1986) 1: 307–310.
19. Ludbrook J: Statistical techniques for comparing measurers and methods of measurement: a critical review. Clin Exp Pharmacol Physiol (2002) 29: 527–536.
20. Bland JM and Altman DG: Comparing methods of measurement: why plotting difference against standard method is misleading. Lancet (1995) 346: 1085–1087.
21. Chen CP and Lin YM: Bland-Altman plots and receiver operating characteristic curves are preferred. Radiology (2010) 257: 896; author reply 896–897.
22. Hilson A: Bland-Altman plot. Radiology (2004) 231: 604; author reply 604–605.
23. Soila KP, Viamonte M, Jr. and Starewicz PM: Chemical shift misregistration effect in magnetic resonance imaging. Radiology (1984) 153: 819–820.
24. Togashi K, Nishimura K, Itoh K, Fujisawa I, Sago T, Minami S, Nakano Y, Itoh H, Torizuka K and Ozasa H: Ovarian cystic teratomas: MR imaging. Radiology (1987) 162: 669–673.
25. Lee SM, Choi YH, Cheon JE, Kim IO, Cho SH, Kim WH, Kim HJ, Cho HH, You SK, Park SH and Hwang MJ: Image quality at synthetic brain magnetic resonance imaging in children. Pediatr Radiol (2017) 47: 1638–1647.
26. Park M, Moon Y, Han SH, Kim HK and Moon WJ: Myelin loss in white matter hyperintensities and normal-appearing white matter of cognitively impaired patients: a quantitative synthetic magnetic resonance imaging study. Eur Radiol (2019) 29: 4914–4921.